

Calculation of the biexciton shift in nanocrystals of inorganic perovskites

T. P. T. Nguyen,^{1,*} S. A. Blundell,^{1,†} and C. Guet^{2,3,‡}

¹*Univ. Grenoble Alpes, CEA, CNRS, IRIG, SyMMES, F-38000 Grenoble, France*

²*Energy Research Institute, Nanyang Technological University, 637141 Singapore*

³*School of Materials Science and Engineering, Nanyang Technological University, 639798 Singapore*

(Dated: February 19, 2020)

We calculate the shift in emission frequency of the trion and biexciton (relative to that of the single exciton) for nanocrystals (NCs) of inorganic perovskites CsPbBr₃ and CsPbI₃. The calculations use an envelope-function $\mathbf{k} \cdot \mathbf{p}$ model combined with self-consistent Hartree-Fock and a treatment of the intercarrier correlation energy in the lowest (second) order of many-body perturbation theory. The carriers in the trion and biexciton are assumed to have relaxed nonradiatively to the ground state at the band edge before emission occurs. The theoretical trion shifts for both CsPbBr₃ and CsPbI₃ are found to be in fair agreement with available experimental data, which include low-temperature single-dot measurements, though are perhaps systematically small by a factor of order 1.5, which can plausibly be explained by a combination of a slightly overestimated dielectric constant and omitted third- and higher-order terms in the correlation energy. Taking this level of agreement into account, we estimate that the ground-state biexciton shift for CsPbBr₃ is a redshift of order 10–20 meV for NCs with an edge-length of 12 nm. This value is intermediate among the numerous high-temperature measurements on NCs of CsPbBr₃, which vary from large redshifts of order 100 meV to blueshifts of several meV.

Keywords: perovskite, nanocrystal, exciton, biexciton, trion, correlation

I. INTRODUCTION

Hybrid organic-inorganic lead halide perovskites such as CH₃NH₃PbX₃ (X = Cl, Br, or I) attracted widespread attention several years ago on account of their excellent properties for photovoltaic applications [1, 2]. The reported power-conversion efficiencies have increased rapidly since then and now reach 23.7% [3]. These high efficiencies are possible in part because the materials have a high defect tolerance [4] and very long carrier diffusion lengths [5].

More recently, nanocrystals (NCs) of all-inorganic lead halide perovskites CsPbX₃ (X = Cl, Br, or I) were shown to be outstanding candidates for light-emitting applications [6]. The NCs fluoresce strongly, with the emission frequency tunable over the entire visible range by varying the size of the NCs and their composition (halide X, including mixtures of different halides) [6]. The quantum yields obtained are close to 100% [7]. This has led to important applications of inorganic perovskite NCs to light-emitting diodes [8, 9], lasers [10, 11], and room-temperature single-photon sources [12], among others.

An important quantity in many light-emitting applications using NCs is the strength of the exciton-exciton interaction, which causes a shift in the frequency of light emitted by a biexciton (two confined excitons) compared to a single exciton. The presence of biexcitons (or, more generally, of multiexcitons) under device conditions can reduce the frequency purity of the emitted light, depending on the size of the shift. The biexciton shift plays

a critical role in lasers based on NCs of II-VI semiconductors such as CdSe, where the small biexciton redshift is instrumental in creating a population inversion on the biexciton-to-exciton transition where lasing occurs [13]. It might also be possible to generate polarization-entangled photon pairs from the biexciton-exciton cascade $|XX\rangle \rightarrow |X\rangle \rightarrow |0\rangle$ in NCs of CsPbBr₃ [12], for which it would help to understand the energetics of the biexciton decay.

However, the biexciton shift in NCs of CsPbBr₃ is at present poorly understood. Many measurements exist [14–19] that largely contradict one another for reasons that are still controversial, with reported values of the biexciton shift varying from large redshifts [16] of order 100 meV to a recently reported small blueshift [19] of order a few meV.

To help understand this issue, we present here calculations of the biexciton shift in NCs of CsPbI₃ and CsPbBr₃ using a multiband $\mathbf{k} \cdot \mathbf{p}$ envelope-function approach, combined with many-body perturbation theory (MBPT). We assume that the biexciton has relaxed nonradiatively (by rapid phonon emission) to its ground state at the band edge before emitting, which enables us to construct a detailed microscopic theory of the multicarrier correlations responsible for the shift. Our results suggest that the biexciton shift under these conditions is a redshift having a value that is intermediate among the available measurements on NCs of CsPbBr₃.

The plan of the paper is the following. In Sec. II we outline our formalism. We treat the confined carriers as an ‘artificial atom’ using methods of MBPT from atomic physics and quantum chemistry [20, 21]. The first step is a self-consistent Hartree-Fock (HF) model of the confined carriers; then we apply the leading correlation correction from second-order MBPT. Our basic envelope-

* phuctan3108@gmail.com

† steven.blundell@cea.fr

‡ cguet@ntu.edu.sg

function model is discussed in Sec. II A, the HF method in Sec. II B, and the correlation energy in Sec. II C. For reasons of computational efficiency, we use a spherical basis set in the MBPT calculations. This leads to extensive formulas for the various terms involving radial integrals and angular factors, which can be derived using standard methods of angular-momentum theory [20, 22, 23]. These detailed formulas will be presented elsewhere.

These methods are then applied to NCs of inorganic perovskites in Sec. III. A difficulty with these materials, which have only recently become the subject of intensive research, is that many of their properties are at present poorly understood. Even some basic properties, such as the effective masses of the valence and conduction bands, are uncertain. We discuss the available data and the parameters that we assume in our model in Sec. III A. Next, in Sec. III B, we apply our approach to the trion and biexciton shift in NCs of CsPbI₃ and CsPbBr₃. Both these shifts are dominated by intercarrier correlation effects, the mean-field (HF) contribution largely canceling [24]. As we shall see, the calculations of the correlation energy for trions and biexcitons are very closely related, so that the data on trion shifts provide a very useful additional check on our calculation of the biexciton shift. Our conclusions are given in Sec. IV.

II. FORMALISM

A. Model

Our approach is based on an envelope-function formalism [25] for a system of carriers (holes and electrons) confined in a potential V_{ext} , with the bulk band structure described by a $\mathbf{k}\cdot\mathbf{p}$ Hamiltonian $h_{\mathbf{k}\cdot\mathbf{p}}$ and screened Coulomb interactions among the carriers. The total Hamiltonian in the space of envelope functions is

$$H = \sum_{ij} \{i^\dagger j\} \langle i | h_{\mathbf{k}\cdot\mathbf{p}} + V_{\text{ext}} | j \rangle + \frac{1}{2} \sum_{ijkl} \{i^\dagger j^\dagger lk\} \langle ij | g_{12} | kl \rangle, \quad (1)$$

where $\{i_1^\dagger i_2^\dagger \dots j_1 j_2 \dots\}$ is a normally ordered product of creation (and absorption) operators for electron envelope states i_1, i_2, \dots (and j_1, j_2, \dots), which span the conduction bands (CBs) and valence bands (VBs) included in the calculation. The Coulomb interaction g_{12} in envelope-function approaches is given generally by a sum of long-range (LR) and short-range (SR) terms [26, 27]. Here we will consider only the LR part (we use atomic units throughout)

$$g_{12} = \frac{1}{\varepsilon_{\text{in}} |\mathbf{r}_1 - \mathbf{r}_2|}, \quad (2)$$

where ε_{in} is the dielectric constant of the NC material appropriate to the length scale L_{dot} of the nanostructure (see Sec. III A). The LR Coulomb interaction is in

principle modified by the mismatch with the dielectric constant ε_{out} of the surrounding medium, which leads to induced polarization charges at the interface, although we will not consider this effect in the present paper.

Even though perovskite NCs are generally cuboid, we use a basis of envelope states i, j, \dots , etc., in Eq. (1) appropriate to spherical symmetry. This is done for reasons of computational efficiency. In a spherical basis, the angular integrals can be carried out analytically and the remaining radial integrals are one-dimensional. It is also possible to sum over the magnetic substates of the basis states analytically [20, 22], which effectively reduces (very substantially) the size of the basis required in correlation calculations. Although we will not do so in this paper, nonspherical terms in the Hamiltonian (for example, arising from the crystal lattice or from the overall shape of the NC) can in principle be included in later stages of the formalism as perturbations.

To generate a spherical basis, we take the confining potential to be spherically symmetric. We choose a spherical well with infinite walls,

$$V_{\text{ext}}(r) = \begin{cases} 0, & \text{if } r < R \\ \infty, & \text{otherwise} \end{cases}. \quad (3)$$

If the NC is a cube with edge-length L , the radius R can be conveniently chosen to satisfy

$$R = L/\sqrt{3}. \quad (4)$$

To motivate this choice of R , we note that at effective-mass level the eigenvalues of noninteracting electrons in a cubic box are given by

$$\epsilon_\lambda^{\text{cube}}(n_x, n_y, n_z) = \frac{\pi^2}{2m_\lambda^* L^2} (n_x^2 + n_y^2 + n_z^2), \quad (5)$$

where (n_x, n_y, n_z) are integers and m_λ^* is the band effective mass. Thus, the condition (4) ensures that the entire spectrum of ‘ S -like’ states in a cube ($n_x = n_y = n_z = n$) coincides exactly with the spectrum of nS states in a sphere,

$$\epsilon_\lambda^{\text{sph}}(n) = \frac{\pi^2 n^2}{2m_\lambda^* R^2}. \quad (6)$$

One can also show that the lowest ‘ P -like’ state in a cube ($n_x = 2, n_y = n_z = 1$, together with the two other permutations, $n_x \leftrightarrow n_y$ and $n_x \leftrightarrow n_z$ [28]) has an energy within 2.3% of that of the $1P$ state in the equivalent sphere (4), and that higher-lying ‘ P -like’ states also have energies within several percent of their analog in the sphere.

Even though the single-particle energies are in close agreement, wave functions and therefore matrix elements can still differ between cubic and spherical confinement. However, in Sec. II B we show that the first-order Coulomb energy of the ground-state exciton differs by only about 1.5% in the two cases, and the HF energy

by about 0.04%. In Sec. II C, we estimate that the error in the correlation energy from using a spherical basis is about 5%. Therefore, for the purposes of this paper, the nonspherical correction term arising from the NC shape is expected to be unimportant.

We consider two $\mathbf{k} \cdot \mathbf{p}$ models. The first is a 4×4 model, which includes the s -like VB and $p_{1/2}$ -like CB around the R point of the Brillouin zone in inorganic perovskite compounds [29, 30]. The other is an 8×8 model including additionally the $p_{3/2}$ -like CB, which lies about 1 eV above the $p_{1/2}$ -like CB at the R point [29–31]. Including the $p_{3/2}$ -like CB in this way leads to a small correction to correlation energies at the 1% level (see Sec. II C).

For spherical confinement, the angular part of an envelope function with orbital angular momentum l couples to a Bloch function with Bloch angular momentum J (here $J = 1/2$ or $3/2$) to give a state with total angular momentum (F, m_F) [32], which we denote by a basis vector $|(l, J)Fm_F\rangle$. In the 8×8 model, the total wave function (including envelope and Bloch functions) can then be written as a sum of four components [32],

$$\begin{aligned} |\eta Fm_F\rangle = & \\ & \frac{g_s(r)}{r} |(l+1, 1/2)Fm_F\rangle + \frac{\bar{g}_p(r)}{r} |(\bar{l}, 1/2)Fm_F\rangle \\ & + \frac{g_p(r)}{r} |(l, 3/2)Fm_F\rangle + \frac{f_p(r)}{r} |(l+2, 3/2)Fm_F\rangle. \end{aligned} \quad (7)$$

Here $g_s(r)$ and $\bar{g}_p(r)$ are the radial envelope functions for the s -like and $p_{1/2}$ -like bands, respectively, while $g_p(r)$ and $f_p(r)$ apply to the $p_{3/2}$ -like band. These last two terms are absent in the 4×4 model. The allowed values of the angular momenta l and \bar{l} follow from angular-momentum and parity selection rules [32]. We solve for the radial functions and eigenvalues of the single-particle states in the presence of a Hartree-Fock potential (Sec. II B) using a generalization of the method of Ref. [32].

For states in the s -like VB, the term involving $g_s(r)$ in Eq. (7) is typically the large component of the wave function, while the other terms are small components representing the admixture of CB states into the VB states due to the finite range of the confining potential V_{ext} and the $\mathbf{k} \cdot \mathbf{p}$ interaction. In the CB states, the role of the small and large components are interchanged. The presence of the small components allows the formalism to pick up the leading $\mathbf{k} \cdot \mathbf{p}$ corrections arising from the coupling of the VB and CB.

B. Hartree-Fock

The first step in the correlation calculation for a general excitonic system with N_e electrons and N_h holes is to solve the self-consistent HF equations including exact exchange [20, 21]. The HF potential will then be used to

define the single-particle states of the many-body procedure discussed in Sec. II C.

For an occupied state $|a\rangle$ (either a hole or an electron), the HF equation is

$$(h_{\mathbf{k}\cdot\mathbf{p}} + V_{\text{ext}} + V_{\text{HF}}^{\text{av}})|a\rangle = \epsilon_a|a\rangle, \quad (8)$$

where the HF potential $V_{\text{HF}}^{\text{av}}$ is given by a sum of direct and exchange terms, $V_{\text{HF}}^{\text{av}} = V_{\text{dir}} + V_{\text{exc}}$, with

$$\langle i|V_{\text{dir}}|a\rangle = \sum_b^{\text{occ}} e_b q_b^a \langle ib|g_{12}|ab\rangle, \quad (9)$$

$$\langle i|V_{\text{exc}}|a\rangle = - \sum_b^{\text{occ}} e_b q_b^a \langle ib|g_{12}|ba\rangle, \quad (10)$$

where the sum is over all occupied (or partially occupied) states. Here e_b is a charge-related parameter, with $e_b = 1$ for electrons and $e_b = -1$ for holes. (We are using the convention that eigenvalues ϵ_a refer to electron states, even though the states may be ‘occupied’ by a hole with an energy $-\epsilon_a$.)

The usual HF potential with $q_b^a = 1$ in Eqs. (9) and (10) is generally only a scalar operator for closed-shell systems. Since we wish to create a spherical basis for open-shell systems as well, we employ instead a *configuration-averaged HF* [20], in which the configuration-averaging weights q_b^a are given by

$$q_b^a = \begin{cases} n_B/g_B & b \notin A \\ (n_B - 1)/(g_B - 1) & b \in A \end{cases}. \quad (11)$$

Here A or B denotes the shell containing the states a or b , respectively, n_B is the occupation number of shell B , and g_B is the degeneracy (maximum occupation) of shell B . For a closed-shell system, $n_B = g_B$ for all shells and then all weights $q_b^a = 1$. The configuration-averaged HF equations (8) for a spherically symmetric V_{ext} can now be reduced to a set of radial HF equations following standard procedures [20].

The configuration-averaged HF energy of the excitonic system is

$$\begin{aligned} E_{\text{HF}}^{\text{av}} = & \sum_a^{\text{occ}} e_a q_a \langle a|h_{\mathbf{k}\cdot\mathbf{p}} + V_{\text{ext}}|a\rangle \\ & + \frac{1}{2} \sum_a^{\text{occ}} e_a q_a \langle a|V_{\text{HF}}^{\text{av}}|a\rangle, \end{aligned} \quad (12)$$

where

$$q_a = n_A/g_A \quad (13)$$

is the fractional occupation of shell A (where $a \in A$). Conventionally we define the zero of the band-structure energy to be the VB maximum. Then we can decompose $E_{\text{HF}}^{\text{av}}$ into different physical contributions as

$$E_{\text{HF}}^{\text{av}} = E_{\text{band}} + E_{\text{conf}} + E_{\text{Coul}}, \quad (14)$$

TABLE I. Hartree-Fock calculation for a ground-state single exciton (X), negative trion (X^-), and biexciton (XX) confined in a NC of CsPbBr₃ with edge-length $L = 9$ nm, using the material parameters in Table III (and $E_P = 20$ eV). E_{band} is the band energy, E_{conf} the confinement energy, E_{dir} and E_{exc} are the direct and exchange Coulomb energy, respectively, E_{Coul} is the total Coulomb energy, $E_{\text{Coul}} = E_{\text{dir}} + E_{\text{exc}}$, and $E_{\text{HF}} = E_{\text{band}} + E_{\text{conf}} + E_{\text{Coul}}$ is the total HF energy.

	X (eV)	X^- (eV)	XX (eV)
E_{band}	2.3420	4.6840	4.6840
E_{conf}	0.1036	0.1556	0.2071
E_{dir}	-0.0699	-0.0069	0.0000
E_{exc}	0.0003	-0.0655	-0.1385
E_{Coul}	-0.0696	-0.0724	-0.1385
E_{HF}	2.3760	4.7671	4.7526

where $E_{\text{band}} = N_e E_g$ is the ‘band energy’ (E_g is the gap between the s -like VB and the $p_{1/2}$ -like CB) and E_{conf} is the confinement energy,

$$E_{\text{conf}} = \sum_a^{\text{occ}} e_a q_a \langle a | h_{\mathbf{k}\cdot\mathbf{p}} | a \rangle - E_{\text{band}}. \quad (15)$$

One can also define an energy of interaction with the external potential, $E_{\text{ext}} = \sum_a^{\text{occ}} e_a q_a \langle a | V_{\text{ext}} | a \rangle$, although here $E_{\text{ext}} \equiv 0$ because of our simple choice of potential (3). The Coulomb energy is

$$E_{\text{Coul}} = \frac{1}{2} \sum_a^{\text{occ}} e_a q_a \langle a | V_{\text{HF}}^{\text{av}} | a \rangle, \quad (16)$$

which can be further decomposed into direct and exchange terms using Eqs. (9) and (10). Example calculations showing these energy contributions for a NC of CsPbBr₃ are given in Table I. Note that the exchange energy for a single exciton is very small; this contribution can be shown to be formally of order $(L_{\text{atom}}/L_{\text{dot}})^2$, where L_{atom} is the interatomic length scale.

To study the dependence of the HF energy on the shape of the NC (sphere or cube), consider the $1S_e$ - $1S_h$ ground state of a single exciton. In the effective-mass limit, the noninteracting $1S$ states (electron or hole) have wave functions

$$\psi_{1S}^{\text{cube}}(\mathbf{r}) = \sqrt{\frac{8}{L^3}} \cos\left(\frac{\pi x}{L}\right) \cos\left(\frac{\pi y}{L}\right) \cos\left(\frac{\pi z}{L}\right) \quad (17)$$

for cubic confinement, and

$$\psi_{1S}^{\text{sph}}(r) = \frac{1}{\sqrt{2\pi R}} \frac{1}{r} \sin\left(\frac{\pi r}{R}\right) \quad (18)$$

for spherical confinement. The confinement (kinetic) energy of the the $1S_e$ - $1S_h$ exciton at this level of approximation follows from Eqs. (4)–(6) to be

$$E_{\text{conf}}^{(1)} = \frac{3\pi^2}{2L^2} \left(\frac{1}{m_e^*} + \frac{1}{m_h^*} \right) \quad (19)$$

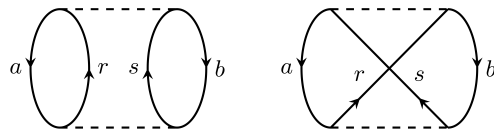


FIG. 1. Closed-shell second-order correlation energy: direct (on the left) and exchange (on the right).

for both the cube and the equivalent sphere (4). The first-order Coulomb energy can be obtained by inserting the wave functions (17) and (18) into Eqs. (9) and (16), and neglecting the exchange term. This gives

$$E_{\text{Coul}}^{(1)} = -\frac{\xi}{\epsilon_{\text{in}} L}, \quad (20)$$

where, after numerical integration, we find $\xi \approx 4.389$ eV nm (for a cube) and $\xi \approx 4.455$ eV nm (for a sphere). Thus, the Coulomb energy differs by about 1.5% between the cube and the equivalent sphere. From Eqs. (14), (19), and (20) we then find that, for the parameters used in Table I, the HF energy of the single exciton at this level of approximation is $E_{\text{HF}} = 2.3858$ eV (for a cube) and $E_{\text{HF}} = 2.3848$ eV (for a sphere), a difference of only 0.04%. Finally, one sees from Table I that the HF energy for a sphere changes by 0.4% from this value upon incorporating $\mathbf{k}\cdot\mathbf{p}$ corrections (with $E_P = 20$ eV) and iterating the HF equations to self-consistency.

C. Correlation energy

From the point of view of MBPT [20, 21], the HF energy of a closed-shell system is correct through first order, $E_{\text{HF}} = E^{(0)} + E^{(1)}$, where $E^{(0)} = \sum_a^{\text{occ}} e_a \epsilon_a$ is the sum of the single-particle eigenvalues of the occupied HF states, and $E^{(1)}$ is the first-order correction of the residual Coulomb interaction. The configuration-averaged HF energy (12) of an open-shell system is similar, but gives the energy of the center of gravity of the configuration multiplet, again correct through first order in MBPT [20]. The higher-order corrections to the energy, $E_{\text{corr}} = E^{(2)} + E^{(3)} + \dots$, are referred to as the *correlation energy*.

In this paper we will consider only the second-order energy, $E_{\text{corr}} \approx E^{(2)}$. For atoms and molecules, $E^{(2)}$ typically accounts for about 75% or more of the total correlation energy (depending on the system)[20, 21] and usually $E^{(2)}/E_{\text{corr}} < 1$. This approximation has the merit of simplicity. Using the spherical basis (7), $E^{(2)}$ for the excitonic systems considered here can be converged to an accuracy of a fraction of a percent in about 1 s or less on a single processing core.

The second-order energy for a closed-shell atom or molecule in a HF potential is given [20, 21] by the many-body diagrams in Fig. 1. To apply this approach to an excitonic system of holes and electrons, we will effectively consider the electrons and holes to be different species

of particle and evaluate the diagram for the mixed system [33]. Thus, the lines directed downward in Fig. 1 (*a* and *b*) correspond to *occupied* states (either holes or electrons) while upward-directed lines (*r* and *s*) correspond to *unoccupied* states (either holes or electrons). The total second-order energy is given by

$$E^{(2)} = \frac{1}{2} \sum_{abrs} D_{abrs}^{(2)}, \quad (21)$$

where

$$D_{abrs}^{(2)} = \frac{\langle ab|g_{12}|rs\rangle(\langle rs|g_{12}|ab\rangle - \langle rs|g_{12}|ba\rangle)}{\omega_a + \omega_b - \omega_r - \omega_s}, \quad (22)$$

and $\omega_i = \epsilon_i$ for electrons and $\omega_i = -\epsilon_i$ for holes, since the single-particle energies must now apply to each particle type. Decomposing $E^{(2)}$ explicitly into electron and hole contributions gives

$$E^{(2)} = E_{ee}^{(2)} + E_{hh}^{(2)} + E_{eh}^{(2)}, \quad (23)$$

where

$$E_{ee}^{(2)} = \frac{1}{2} \sum_{abrs}^{\text{elec}} D_{abrs}^{(2)}, \quad E_{hh}^{(2)} = \frac{1}{2} \sum_{abrs}^{\text{hole}} D_{abrs}^{(2)},$$

$$E_{eh}^{(2)} = \sum_{\substack{ar \text{ (elec)} \\ bs \text{ (hole)}}} D_{abrs}^{(2)}. \quad (24)$$

The terms $E_{ee}^{(2)}$ and $E_{hh}^{(2)}$ correspond to the correlation energy of the separate electron and hole subsystems, respectively. The third term $E_{eh}^{(2)}$ is a cross-term, involving single excitations of both the electron and hole subsystems.

A general excitonic system with N_e electrons and N_h holes may contain open shells. An approximate formula for the correlation energy in this case may be found by inserting configuration-averaging weights for the occupied or partially occupied shells of *a* and *b* into the closed-shell formula (21), following the same argument used for the configuration-averaged HF energy [20]. Equation (21) is then modified by

$$D_{abrs}^{(2)} \rightarrow q_a q_b^a D_{abrs}^{(2)}, \quad (25)$$

where q_b^a and q_a are given by Eqs. (11) and (13), respectively.

To evaluate the sums over states in Eq. (21), we create a basis set of single-particle states in the HF potential (8) up to a high energy cutoff. This basis set contains the occupied or partially occupied states *a* and *b*, which contribute to the HF potential, together with unoccupied (excited) states *r* and *s*. For the calculations on single excitons, trions, and biexcitons presented in this paper, we take q_b^a for any *unoccupied* state *a* to be q_b^c , where *c* is chosen to be the $1S_e$ state (for electrons) or the $1S_h$

TABLE II. Second-order correlation energy for a ground-state single exciton (*X*), negative trion (X^-), and biexciton (*XX*) confined in a NC of CsPbBr₃ with edge-length $L = 9$ nm, using the material parameters in Table III (and $E_P = 20$ eV). $E_{ee}^{(2)}$, $E_{hh}^{(2)}$, and $E_{eh}^{(2)}$ are the electron term, the hole term, and the electron-hole cross-term, respectively, given by Eq. (24). Direct (dir) and exchange (exc) terms are shown separately; the exchange term from $E_{eh}^{(2)}$ is negligible. First three columns: $4 \times 4 \mathbf{k} \cdot \mathbf{p}$ model; last column: $8 \times 8 \mathbf{k} \cdot \mathbf{p}$ model. Units: meV.

	$4 \times 4 \mathbf{k} \cdot \mathbf{p}$			$8 \times 8 \mathbf{k} \cdot \mathbf{p}$
	<i>X</i>	X^-	<i>XX</i>	<i>X</i>
$E_{ee}^{(2)}$ (dir)	0.00	-8.44	-8.41	0.00
$E_{ee}^{(2)}$ (exc)	0.00	4.21	4.20	0.00
$E_{hh}^{(2)}$ (dir)	0.00	0.00	-8.41	0.00
$E_{hh}^{(2)}$ (exc)	0.00	0.00	4.20	0.00
$E_{eh}^{(2)}$ (dir)	-6.83	-10.22	-16.82	-7.13
$E_{eh}^{(2)}$ (total)	-6.83	-14.44	-25.24	-7.13

state (for holes). This choice forces all *S*-wave excited states in the basis set to be orthogonal to the occupied $1S_e$ and $1S_h$ states (as required).

Example calculations of the second-order correlation energy are given in Table II. Note that only the cross-term $E_{eh}^{(2)}$ contributes for a single exciton, since the configuration-averaging weights in Eq. (25) vanish for the other terms. Also, the electron $E_{ee}^{(2)}$ and hole $E_{hh}^{(2)}$ terms here contribute equally for the biexciton, because we assume VB-CB symmetry in the material parameters; this is not true in general. The sums over the intermediate states *r* and *s* are quite rapidly convergent: about 10% of $E^{(2)}$ arises from the *S*-wave channel, 70% from the *P*-wave channel, and 18% from the *D*- and *F*-wave channels. In addition, the first three principal quantum numbers of each angular channel are sufficient to obtain about 98% of $E^{(2)}$. We note that the contributions to $E^{(2)}$ presented contain small $\mathbf{k} \cdot \mathbf{p}$ corrections of about 2%.

From Table II, we see that using the $8 \times 8 \mathbf{k} \cdot \mathbf{p}$ model modifies the single-exciton correlation energy by only about 4% compared to the 4×4 model. Actually, most of this shift is due to the modification of the $\mathbf{k} \cdot \mathbf{p}$ corrections by the presence of the $p_{3/2}$ -like band. If the calculations are repeated in the effective-mass limit ($E_P \rightarrow 0$), one finds a difference of only about 0.1% between the 8×8 and 4×4 models, showing that the excitations into the $p_{3/2}$ -like band are not very significant in themselves (owing to their relatively high excitation energy). This justifies the use of the $4 \times 4 \mathbf{k} \cdot \mathbf{p}$ model for perovskite NCs for the calculation of the correlation energy.

Noting that the dominant intermediate channel is *P*-wave, we estimate the error in $E^{(2)}$ from using a spherical (not cubic) basis to be about 5%, which is the error in the energy denominator associated with the $1S \rightarrow nP$ excitations for $n = 1-3$ (see Sec. II A).

For an alternative approach to correlation in a confined

TABLE III. Parameters used in the calculations. $E_P^{(1)}$ is the Kane parameter estimated from the $4 \times 4 \mathbf{k} \cdot \mathbf{p}$ model, $E_P^{(2)}$ from the $8 \times 8 \mathbf{k} \cdot \mathbf{p}$ model. For further explanation, see Sec. III A.

	CsPbBr ₃	CsPbI ₃
E_g (eV)	2.342 ^a	1.723 ^a
μ^* (m_0)	0.126 ^a	0.114 ^a
m_e^*, m_h^* (m_0)	0.252	0.228
Δ_{soc} (eV)	1.0 ^b	1.0 ^b
ε_{eff}	7.3 ^a	10.0 ^a
ε_{opt}	5.3 ^c	4.8 ^d
$E_P^{(1)}$ (eV)	27.9	22.7
$E_P^{(2)}$ (eV)	16.4	13.9

^a Ref. [35]

^b Ref. [31]

^c Ref. [36], at a wavelength of 600 nm.

^d Ref. [37], at a wavelength of 600 nm.

excitonic system with spherical symmetry, see Ref. [34].

III. APPLICATION TO PEROVSKITE NANOCRYSTALS

A. Parameters

The material parameters that we use for CsPbBr₃ and CsPbI₃ are summarized in Table III. The bulk parameters μ^* and ε_{eff} are taken from Ref. [35] and apply to the orthorhombic phase of CsPbBr₃ and the cubic phase of CsPbI₃ at cryogenic temperatures [38–40]. Although the reduced mass $\mu^* = m_e^* m_h^* / (m_e^* + m_h^*)$ has been measured [35] by magneto-transmission techniques, the individual effective masses of electron m_e^* and hole m_h^* are unknown. Evidence from experiment [41] and first-principles calculations [6, 30, 42] suggests, however, that m_e^* and m_h^* are approximately equal. Here we will assume $m_e^* = m_h^*$ exactly (m_e^* applies to the $p_{1/2}$ -like CB, and m_h^* to the s -like VB, around the R point of the Brillouin zone). The spin-orbit splitting Δ_{soc} between the $p_{1/2}$ -like and the higher-lying $p_{3/2}$ -like band has been measured in Ref. [31].

The ‘effective’ dielectric constant ε_{eff} in Table III is derived [35] from the measured binding energy of the bulk exciton. We also give for comparison values of the optical dielectric constant ε_{opt} at a wavelength of 600 nm, which are somewhat smaller than ε_{eff} . The constant ε_{eff} applies to a length scale of order the bulk Bohr radius a_B , which is quite close to the size of the NCs that we consider ($2a_B = 6.1$ nm for CsPbBr₃ and $2a_B = 9.3$ nm for CsPbI₃, using the parameters in Table III). Therefore we shall use $\varepsilon_{\text{in}} = \varepsilon_{\text{eff}}$ to screen the LR Coulomb interaction (2) in the main parts of our calculations of the correlation and exchange energy.

The Kane parameter E_P of CsPbBr₃ and CsPbI₃ has not been measured directly. An estimate of E_P can be made by assuming that the contribution to m_e^* and m_h^* from remote bands is zero, which in the $8 \times 8 \mathbf{k} \cdot \mathbf{p}$ model

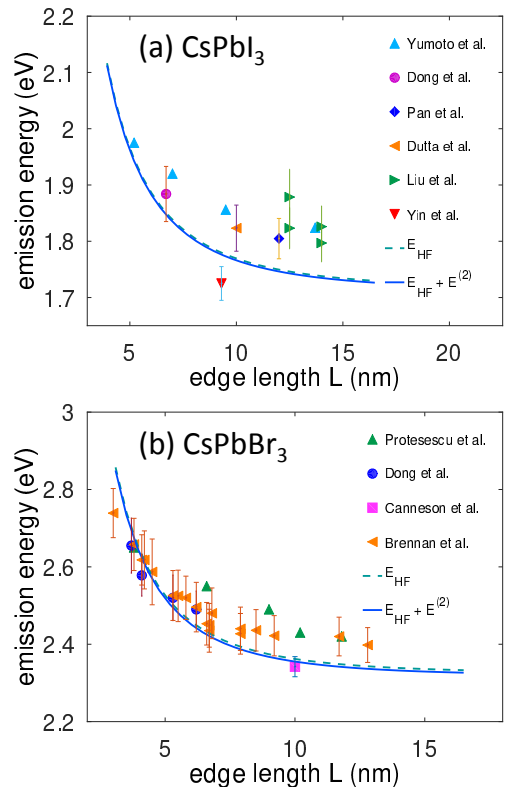


FIG. 2. Measured photoluminescence peak energies of NCs of (a) CsPbI₃ and (b) CsPbBr₃ (triangles/squares/circles), and theoretical single-exciton energy using HF (dashed curve) and HF plus second-order correlation energy (full curve). Yumoto *et al.*, Ref. [43]; Dong *et al.*, Ref. [44]; Pan *et al.*, Ref. [45]; Dutta *et al.*, Ref. [46]; Liu *et al.*, Ref. [47]; Yin *et al.*, Ref. [48]; Protesescu *et al.*, Ref. [6]; Cannesson *et al.*, Ref. [49]; Brennan *et al.*, Ref. [50].

implies [51]

$$\frac{1}{\mu^*} = \frac{2}{3} \left(\frac{E_P}{E_g} + \frac{E_P}{E_g + \Delta_{\text{soc}}} \right), \quad (26)$$

where E_g is the gap energy. The Kane parameter here is defined by

$$E_P = 2|\langle S|p_z|Z \rangle|^2, \quad (27)$$

where $|S\rangle$ is the Bloch state of the s -like band and $|Z\rangle$ is the z -component of the Bloch state of the (spin-uncoupled) p -like band [52]. Equation (26) can now be solved for E_P . The corresponding equation [29, 35] for the $4 \times 4 \mathbf{k} \cdot \mathbf{p}$ model is obtained by allowing $\Delta_{\text{soc}} \rightarrow \infty$. The values of E_P inferred in this way for the two models are summarized in Table III.

We take the view that E_P is uncertain. A conservative range would be $10 \text{ eV} \leq E_P \leq 32 \text{ eV}$ for CsPbBr₃ and $8 \text{ eV} \leq E_P \leq 26 \text{ eV}$ for CsPbI₃. Note that the uncertainty in E_P is not critical for the calculation of the energy, since E_P determines only the rather small $\mathbf{k} \cdot \mathbf{p}$ corrections to $E_{\text{HF}}^{\text{av}}$ and E_{corr} (see Secs. II B and II C).

For illustrative purposes, we choose a central value of $E_P = 20$ eV for CsPbBr₃ in Tables I and II.

An overall assessment of the parameters and the model can be made by comparing the theoretical single-exciton energy with the energy of the emission peak [53], as shown in Fig. 2. The data in the figure correspond to a variety of experimental conditions. Most of the measurements were made at room temperature, although Yin *et al.* [48] (CsPbI₃) and Canneson *et al.* [49] (CsPbBr₃) were at cryogenic temperatures, as were the measurements [35] used to determine our parameters (Table III), which are therefore more appropriate to low temperatures. This explains part of the apparent small discrepancy at large sizes L , as the bandgap increases at room temperature by about 60 meV (CsPbBr₃) to 80 meV (CsPbI₃) [35]. Also, the measurement of Liu *et al.* [47] (CsPbI₃) is ligand-dependent, as indicated by the multiple data points.

It is clear from Fig. 2 that the contribution of correlation to the total emission frequency is not significant, but the role of correlation is greatly enhanced in measurements of the trion and biexciton shifts, which are discussed in the next section.

B. Bi-exciton and trion shifts

Emission from trions or biexcitons in NCs is usually observed to occur at a slightly lower frequency than from a single exciton [16, 17, 24, 54, 55]. The trion Δ_{X^-} and biexciton Δ_{XX} redshifts, relative to the single-exciton emission frequency, can be found by taking the difference of the initial and final energies,

$$\Delta_{XX} = 2E_X - E_{XX}, \quad (28)$$

$$\Delta_{X^-} = E_X + E_{1e} - E_{X^-}, \quad (29)$$

where E_X , E_{X^-} , E_{XX} , and E_{1e} are the total energies of the single exciton, the negative trion, the biexciton, and a single confined electron, respectively. We assume here that the excitonic systems relax nonradiatively under experimental conditions before emitting, so that these total energies will be taken to refer to the ground state. In Eqs. (28) and (29), we have anticipated that the shifts are redshifts by defining Δ_{X^-} and Δ_{XX} as minus the change in energy relative to a single exciton. Because we assume VB-CB symmetry of effective-mass parameters (see Table III), the positive trion will have an identical shift to the negative trion, $\Delta_{X^+} = \Delta_{X^-}$.

Remarkably, the biexciton [Eq. (28)] and trion [Eq. (29)] shifts are dominated by intercarrier correlation effects, as the mean-field contribution largely cancels [24]. This phenomenon for a NC of CsPbBr₃ is illustrated in Table IV. Note that for large edge-lengths $L \gtrsim 7$ nm, the cancelation of the HF contribution is more complete for the biexciton than for the trion, with the reverse being true for the smaller edge-lengths tabulated. The final shifts Δ_{XX} and Δ_{X^-} have a quite weak size dependence. This can be understood by noting that a Coulomb matrix element scales approximately as $\langle ab|g_{12}|rs\rangle \sim 1/L$, while

TABLE IV. Calculated biexciton Δ_{XX} and trion Δ_{X^-} redshifts in NCs of CsPbBr₃ with edge-lengths $4 \text{ nm} \leq L \leq 12 \text{ nm}$, assuming the material parameters in Table III (and $E_P = 20$ eV). The contributions to Eqs. (28) and (29) from Hartree-Fock (HF) and correlation (Corr) are shown separately; Δ_{XX} and Δ_{X^-} are the sum of the HF and Corr terms. Units: meV.

	4 nm	6 nm	9 nm	12 nm
HF	-3.96	-1.57	-0.58	-0.28
Corr	18.16	14.68	11.58	9.62
Δ_{XX}	14.19	13.11	11.00	9.34
HF	-0.05	1.03	1.41	1.47
Corr	10.84	9.15	7.61	6.50
Δ_{X^-}	10.79	10.18	9.02	7.96

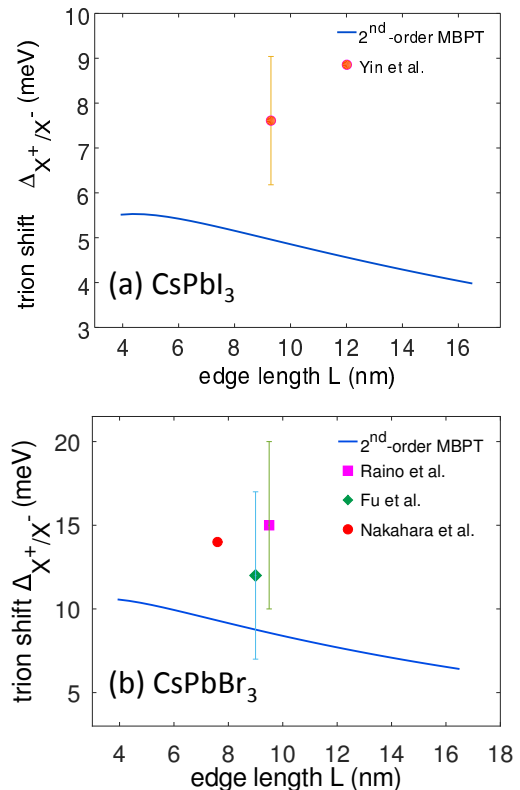


FIG. 3. Measured trion redshift Δ_{X^-} of NCs of (a) CsPbI₃ and (b) CsPbBr₃ (squares/circles/diamonds). Solid line: theory (second-order MBPT). Yin *et al.*, Ref. [48]; Rainò *et al.*, Ref. [55]; Fu *et al.*, Ref. [56]; Nakahara *et al.*, Ref. [54].

the energy denominator in Eq. (22) scales approximately as $\omega_a + \omega_b - \omega_r - \omega_s \sim 1/L^2$ owing to the confinement effect (5), so that $E^{(2)}$ is approximately independent of L . In fact, both Δ_{XX} and Δ_{X^-} become slightly larger at the smaller sizes in Table IV, an effect that has been observed experimentally in perovskite NCs [16].

Our theoretical trion shifts are compared with the available experimental data in Fig. 3. The agreement with the trion data is fair, although the theoretical values are perhaps systematically too small (by a factor

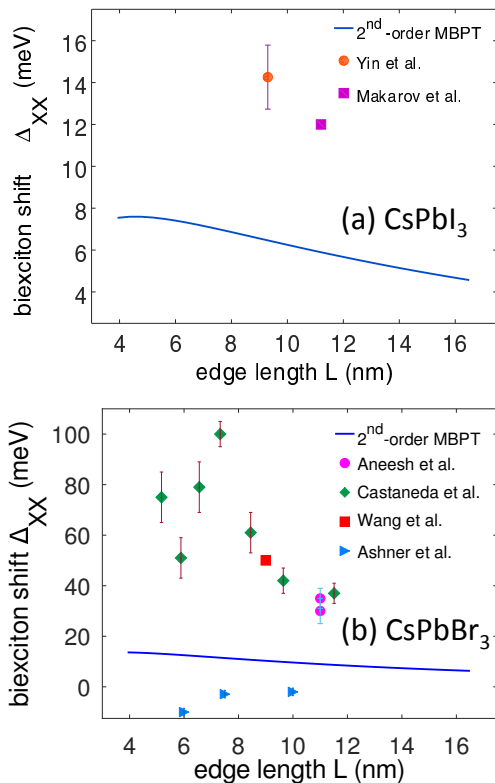


FIG. 4. Measured biexciton redshift Δ_{XX} of NCs of (a) CsPbI₃ and (b) CsPbBr₃ (triangles/squares/circles/diamonds). Solid line: theory (second-order MBPT). Yin *et al.*, Ref. [48]; Makarov *et al.*, Ref. [15]; Aneesh *et al.*, Ref. [17]; Castaneda *et al.*, Ref. [16]; Wang *et al.* Ref. [14]; Ashner *et al.*, Ref. [19].

of order 1.3–1.8). Turning to the data on the biexciton shift, shown in Fig. 4, we see that a similar comment holds for CsPbI₃, where the theoretical values are smaller than the few available measurements by a factor of about 1.8–2.0. The situation is rather unclear for the biexciton shift in CsPbBr₃, however, where there are more data available. The measured values of Δ_{XX} for CsPbBr₃ range from large redshifts [16] of about 40–100 meV (which is comparable to the HF Coulomb energy given in Table I) to a recently reported small blueshift [19], of order $\Delta_{XX} = -2$ meV for $L \approx 10$ nm. Our second-order MBPT approach predicts a redshift for all sizes considered for both CsPbBr₃ and CsPbI₃, with a value $\Delta_{XX} = 10$ meV for CsPbBr₃ for $L \approx 10$ nm.

Before commenting on the experimental data, let us first review some leading sources of theoretical error in our second-order MBPT approach. These are:

(i) *Correction terms due to fine-structure splittings.* We have neglected the fine structure (FS) of the excitonic states, basing our formalism on a configuration-averaged approach (25), which yields the center of gravity of the FS multiplet. FS splittings in emission lines of inorganic perovskite NCs are observed to vary from several hundred μeV (e.g., Ref. [48]) to a few meV (e.g.,

Ref. [30]). Single-dot spectroscopy reveals that they can vary quite markedly from dot to dot, both in magnitude and sometimes also in the number of FS components observed [30, 48, 56]. In the few cases that FS splittings have been observed experimentally in the measurements relevant to Figs. 3 and 4, the shifts plotted in the figures correspond to the values obtained by averaging over the FS (e.g., Ref. [48]). Because of this and the relatively small size of the FS splittings, the error in Figs. 3 and 4 due to FS seems likely to be at the level of 1–2 meV or less.

Let us consider the role of the FS of the single exciton in greater detail. In perovskite NCs, the ground-state $1S_e-1S_h$ single exciton consists of electron and hole states with angular momentum $F = 1/2$, in the notation of Eq. (7), which can couple to a total angular momentum $F_{\text{tot}} = 0$ or 1 (singlet or triplet, respectively). The triplet state has an allowed electric-dipole radiative decay and is a bright exciton state; the singlet is a dark state [30, 56]. Similarly, the ground-state biexciton in perovskite NCs has closed-shell electron and hole states, $1S_e^2-1S_h^2$, which must therefore couple to $F_{\text{tot}} = 0$, and the negative trion has a $1S_e^2-1S_h$ ground state with $F_{\text{tot}} = 1/2$. From selection rules, the allowed biexciton emission must proceed via the bright single-exciton state, $XX_0 \rightarrow X_1$, where the subscript indicates the value of F_{tot} .

Now, the center of gravity of the bright-dark FS multiplet in the single exciton is given by

$$\bar{E}_X = (1/4)E_{X_0} + (3/4)E_{X_1}, \quad (30)$$

from which it follows that $E_{X_1} - \bar{E}_X = \Delta_{10}/4$, where $\Delta_{10} = E_{X_1} - E_{X_0}$ is the bright-dark FS splitting. (We are assuming that any FS in the bright state, which is due to nonspherical or noncubic symmetry-breaking interactions [30, 56–58], has been experimentally averaged.) For the biexciton, the configuration-averaged energy $\bar{E}_{XX} = E_{XX_0}$, since there is only one state. Therefore, the observed biexciton shift is given by

$$\Delta_{XX} = 2E_{X_1} - E_{XX_0} = (2\bar{E}_X - \bar{E}_{XX}) + \Delta_{10}/2, \quad (31)$$

and we see that our calculated result in Fig. 4 acquires a correction term $\Delta_{10}/2$. An analogous argument leads to a correction term $\Delta_{10}/4$ for the trion shift in Fig. 3. Since $|\Delta_{10}|$ is expected to be of order a few meV [58], we conclude again that any error in Figs. 3 and 4 from this source is likely to be of order at most 1–2 meV.

(ii) *Uncertainty in the value of the dielectric constant.* The biexciton Δ_{XX} and trion Δ_X - shifts are dominated by correlation or $E^{(2)}$, so that they are both approximately proportional to $1/\epsilon_{\text{in}}^2$, where ϵ_{in} is the dielectric constant of the material (2). However, a more complete treatment of dielectric effects than considered in the present paper would take into account the space- and frequency-dependent bulk dielectric function $\epsilon(\mathbf{k}, \omega)$. In the instantaneous approximation $\omega = 0$, the dielectric constant ϵ_{in} in Eq. (2) would then be replaced by a space-dependent function $\epsilon(\mathbf{r}_1, \mathbf{r}_2)$. A more general treatment

including also the frequency-dependence of $\varepsilon(\mathbf{k}, \omega)$ would require a retarded Coulomb interaction (and, for example, the use of Feynman propagators [59]). Inorganic perovskites present the complication that the dielectric function is rapidly varying; for instance, the effective and optical dielectric constants given in Table III are quite different.

Another dielectric effect, which we have neglected here, arises from the mismatch of the dielectric constant of the NC with that of the surroundings, which modifies the effective LR Coulomb interaction to take account of polarization charges induced at the dielectric boundary [60].

In our calculations, we have assumed a dielectric constant $\varepsilon_{\text{in}} = \varepsilon_{\text{eff}}$, where ε_{eff} is derived from the measured binding energy of the bulk exciton (see Sec. III A). Formally, ε_{eff} corresponds to length scales of order the Bohr radius $k \sim \pi/a_B$ and to a frequency $\omega \approx 0$, since the exciton binding energy is dominated by the direct Coulomb energy (9) and (16), in which the energy flowing through the Coulomb propagator in the Feynman rules is zero. The second-order energy $E^{(2)}$, on the other hand, involves a nonzero average excitation energy $\delta\omega_{\text{av}} = \langle \omega_a + \omega_b - \omega_r - \omega_s \rangle$ in Eq. (25), which implies a nonzero average energy flowing through the Coulomb propagators. We find $\delta\omega_{\text{av}} \approx 0.1\text{--}0.6$ eV for $4 \text{ nm} \leq L \leq 12 \text{ nm}$ for NCs of CsPbBr₃. In addition, although the size of our NCs is comparable to the Bohr radius (see Sec. III A), this is not exactly true. It follows that the appropriate value of the dielectric constant ε_{in} to use in calculations of $E^{(2)}$ might differ from ε_{eff} . For instance, it seems likely that the frequency-dependence will shift the appropriate value of ε_{in} from ε_{eff} toward a slightly smaller value, closer to ε_{opt} (see Table III). This would increase $E^{(2)}$ and could explain part of the discrepancy between theory and experiment observed in Figs. 3 and 4(a).

(iii) *Higher-order correlation.* Usually in atoms and molecules, $E^{(2)}$ underestimates the all-order correlation energy [20, 21]. Unfortunately, it is hard to estimate the higher-order correlation $E^{(3+)} = E^{(3)} + E^{(4)} + \dots$ without explicit calculation, although we note that typical values of $E^{(3+)}$ for atoms and molecules can vary up to 25% or so of $E^{(2)}$, depending on the system. Each order of MBPT brings in one extra Coulomb interaction g and an energy denominator $\Delta\epsilon$, which scale approximately as $g/\Delta\epsilon \sim L$. Therefore the contribution of higher-order MBPT is expected to become more important for larger dots, and this could explain a large part of the discrepancies noted in Figs. 3 and 4(a) for the case of intermediate confinement encountered in perovskite NCs.

Table II makes it clear that the calculations of $E^{(2)}$ for the trion and the biexciton are very closely related. The term $E_{ee}^{(2)}$ in Eq. (23) can be seen to have almost the same value for each. This happens because both systems contain two electrons, so that the configuration-averaging factors in Eq. (25) are the same (although the basis sets differ slightly, because different states are occupied in

the HF potential of the two systems). Similarly, most of the difference in the other two terms $E_{eh}^{(2)}$ and $E_{hh}^{(2)}$ in Table II is due simply to the different configuration-averaging weights for the trion and biexciton. Because of this, we expect that the errors in Δ_{XX} and Δ_{X-} due to both dielectric effects [(ii) above] and omitted higher-order MBPT [(iii) above] should be comparable. The trion data in Fig. 3 can therefore serve as an additional check on the biexciton data in Fig. 4.

Turning to the experimental data, we note first that it is useful to distinguish between measurements on single dots at cryogenic temperatures (e.g., using time-resolved photoluminescence) and high-temperature measurements on ensembles of NCs (e.g., using transient absorption). The low-temperature measurements typically give narrow well-separated peaks, from which the shifts can be extracted directly, while the high-temperature measurements typically require extensive fits to side-features on overlapping peaks, or other indirect analysis methods. Low-temperature single-dot measurements have been performed on the trion (Fig. 3) by Fu *et al.* [56] for CsPbBr₃ and by Yin *et al.* [48] for CsPbI₃, and the latter also measured the biexciton shift for CsPbI₃ (Fig. 4a). No low-temperature measurements are available of the biexciton shift in CsPbBr₃.

We observe that our agreement with all these low-temperature measurements in the trion shift (Fig. 3) is fair. Based on this, and the observation that the theoretical errors for the trion and the biexciton shift are expected to be similar, we believe that the present results provide quite strong theoretical evidence that the ground-state biexciton shift in NCs of CsPbBr₃ is a red-shift of order $\Delta_{XX} = 10\text{--}20$ meV for $L \approx 12$ nm (after allowing for a phenomenological increase in the second-order MBPT values given in Table IV by a factor of up to 2).

According to Shulenberger *et al.* [18], who performed experiments on NCs of CsPbBr₃, the fast red-shifted features often attributed to biexciton emission are actually an artifact of the exposure of the sample to air, which they claim causes the formation of larger bulk-like particles in the ensemble with a red-shifted single-exciton peak. Shulenberger *et al.* [18] placed an upper limit on the true biexciton shift of 20 meV, which is consistent with our theoretical prediction. However, the same group later inferred [19] a small biexciton *blueshift* of order $\Delta_{XX} = -2$ meV for $L \approx 10$ nm after extensive data fitting, which seems to be inconsistent with our theoretical value.

Another experimental issue is whether the biexciton has truly relaxed to the ground state, as we have assumed in our calculation. Yumoto *et al.* [43] studied ‘hot’ biexcitons in a transient absorption experiment on NCs of CsPbI₃ by observing the induced absorption signal immediately after the pump excitation. They concluded that a hot biexciton, composed of one exciton at the band edge and a second excited exciton, had a substantially increased exciton-exciton interaction. They found

that Δ_{XX} for CsPbI₃ could be as large as 60 meV for excitation energies E_{ex} of the second exciton of order $E_{\text{ex}} \gtrsim 0.3$ eV.

Finally, we note that Makarov *et al.* [15] measured $\Delta_{XX} = 12$ meV for NCs of CsPbI₃ and obtained almost the same value $\Delta_{XX} = 11$ meV for NCs of the mixed perovskite CsPbI_{1.5}Br_{1.5}, which would imply a biexciton shift for CsPbBr₃ in agreement with our theoretical value.

IV. CONCLUSIONS

We have presented a calculation of the trion and biexciton shifts in NCs of CsPbI₃ and CsPbBr₃ using second-order MBPT. The agreement with the available data for the biexciton shift in CsPbI₃ and the trion shift in both CsPbI₃ and CsPbBr₃ is fair, although the theoretical values seem to be systematically slightly smaller than the measurements, a result that can be plausibly understood in terms of a slightly overestimated dielectric constant and omitted higher-order terms in MBPT. After taking this level of agreement between theory and experiment into account, we infer that the ground-state biexciton shift in NCs of CsPbBr₃ is a redshift with a value of order 10–20 meV (for a size $L = 12$ nm). This value is intermediate in the large range of measured values for CsPbBr₃.

The theoretical approach used can be improved in various ways in future work. It is possible to include higher-

order MBPT for excitonic systems with few carriers by means of all-order procedures such as full configuration interaction [21]. A better understanding of the dielectric function in perovskites could perhaps be obtained using *ab initio* atomistic codes [61]. The LR Coulomb interaction (2) can also be generalized to take account of the dielectric mismatch with the surrounding medium [60]. Although envelope-function methods naturally work better on larger NCs, where atomistic effects are relatively less significant, an important atomistic effect can be included straightforwardly by assuming a diffuse finite surface barrier instead of an abrupt infinite barrier (3). Also, explicit nonspherical corrections for the cubic NC shape could be added as perturbations.

Finally, it should be possible to generalize the methods presented here to study hot biexcitons, in which one or both excitons are excited. It would also be interesting to study thermal effects on the biexciton shift at high temperature, a regime that is more relevant to the conditions found in practical devices. The present paper assumes that the excitonic systems are in their quantum ground state, so that it is perhaps natural to expect better agreement with the low-temperature data.

ACKNOWLEDGMENTS

The authors would like to thank Sum Tze Chien for helpful discussions. TN and SB gratefully acknowledge Frédéric Schuster of the CEA's PTMA for support.

-
- [1] M. Z. Liu, M. B. Johnston, and H. J. Snaith, Efficient planar heterojunction perovskite solar cells by vapour deposition, *Nature* **501**, 395 (2013).
 - [2] T. Baikie, Y. N. Fang, J. M. Kadro, M. Schreyer, F. X. Wei, S. G. Mhaisalkar, M. Graetzel, and T. J. White, Synthesis and crystal chemistry of the hybrid perovskite (CH₃NH₃)PbI₃ for solid-state sensitised solar cell applications, *J. Mater. Chem. A* **1**, 5628 (2013).
 - [3] Q. Jiang, Z. N. Chu, P. Y. Wang, X. L. Yang, H. Liu, Y. Wang, Z. G. Yin, J. L. Wu, X. W. Zhang, and J. B. You, Planar-structure perovskite solar cells with efficiency beyond 21%, *Adv. Mater.* **29**, 1703852 (2017).
 - [4] J. Kang and L. W. Wang, High defect tolerance in lead halide perovskite CsPbBr₃, *J. Phys. Chem. Lett.* **8**, 489 (2017).
 - [5] A. A. Zhumekenov, M. I. Saidaminov, M. A. Haque, E. Alarousu, S. P. Sarmah, B. Murali, I. Dursun, X. H. Miao, A. L. Abdelhady, T. Wu, O. F. Mohammed, and O. M. Bakr, Formamidinium lead halide perovskite crystals with unprecedented long carrier dynamics and diffusion length, *ACS Energy Lett.* **1**, 32 (2016).
 - [6] L. Protesescu, S. Yakunin, M. I. Bodnarchuk, F. Krieg, R. Caputo, C. H. Hendon, R. X. Yang, A. Walsh, and M. V. Kovalenko, Nanocrystals of cesium lead halide perovskites (CsPbX₃, X = Cl, Br, and I): Novel optoelectronic materials showing bright emission with wide color gamut, *Nano Lett.* **15**, 3692 (2015).
 - [7] F. Krieg, S. T. Ochsenein, S. Yakunin, S. ten Brinck, P. Aellen, A. Suess, B. Clerc, D. Guggisberg, O. Nazarenko, Y. Shynkarenko, S. Kumar, C. J. Shih, I. Infante, and M. V. Kovalenko, Colloidal CsPbX₃ (X = Cl, Br, I) nanocrystals 2.0: Zwitterionic capping ligands for improved durability and stability, *ACS Energy Lett.* **3**, 641 (2018).
 - [8] W. Deng, X. Z. Xu, X. J. Zhang, Y. D. Zhang, X. C. Jin, L. Wang, S. T. Lee, and J. S. Jie, Organometal halide perovskite quantum dot light-emitting diodes, *Adv. Funct. Mater.* **26**, 4797 (2016).
 - [9] G. R. Li, F. W. R. Rivarola, N. J. L. K. Davis, S. Bai, T. C. Jellicoe, F. de la Pena, S. C. Hou, C. Ducati, F. Gao, R. H. Friend, N. C. Greenham, and Z. K. Tan, Highly efficient perovskite nanocrystal light-emitting diodes enabled by a universal crosslinking method, *Adv. Mater.* **28**, 3528 (2016).
 - [10] J. Pan, S. P. Sarmah, B. Murali, I. Dursun, W. Peng, M. R. Parida, J. Liu, L. Sinatra, N. Alyami, C. Zhao, E. Alarousu, T. K. Ng, B. S. Ooi, O. M. Bakr, and O. F. Mohammed, Air-stable surface-passivated perovskite quantum dots for ultra-robust, single- and two-photon-induced amplified spontaneous emission, *J. Phys. Chem. Lett.* **6**, 5027 (2015).
 - [11] S. Yakunin, L. Protesescu, F. Krieg, M. I. Bodnarchuk, G. Nedelcu, M. Humer, G. De Luca, M. Fiebig, W. Heiss, and M. V. Kovalenko, Low-threshold am-

- plified spontaneous emission and lasing from colloidal nanocrystals of caesium lead halide perovskites, *Nat. Commun.* **6**, 8056 (2015).
- [12] H. Utzat, W. W. Sun, A. E. K. Kaplan, F. Krieg, M. Ginterseder, B. Spokoyny, N. D. Klein, K. E. Shulenberger, C. F. Perkinson, M. V. Kovalenko, and M. G. Bawendi, Coherent single-photon emission from colloidal lead halide perovskite quantum dots, *Science* **363**, 1068 (2019).
- [13] J. Nanda, S. A. Ivanov, M. Achermann, I. Bezel, A. Piryatinski, and V. I. Klimov, Light amplification in the single-exciton regime using exciton-exciton repulsion in type-II nanocrystal quantum dots, *J. Phys. Chem. C* **111**, 15382 (2007).
- [14] Y. Wang, X. Li, J. Song, L. Xiao, H. Zeng, and S. H., All-inorganic colloidal perovskite quantum dots: A new class of lasing materials with favorable characteristics, *Adv. Mater.* **27**, 7101 (2015).
- [15] N. S. Makarov, S. J. Guo, O. Isaienko, W. Y. Liu, I. Robel, and V. I. Klimov, Spectral and dynamical properties of single excitons, biexcitons, and triions in cesium-lead-halide perovskite quantum dots, *Nano Lett.* **16**, 2349 (2016).
- [16] J. A. Castaneda, G. Nagamine, E. Yassitepe, L. G. Bonato, O. Voznyy, S. Hoogland, A. F. Nogueira, E. H. Sargent, C. H. B. Cruz, and L. A. Padilha, Efficient biexciton interaction in perovskite quantum dots under weak and strong confinement, *ACS Nano* **10**, 8603 (2016).
- [17] J. Aneesh, A. Swarnkar, V. Kumar Ravi, R. Sharma, A. Nag, and K. V. Adarsh, Ultrafast exciton dynamics in colloidal CsPbBr₃ perovskite nanocrystals: Biexciton effect and Auger recombination, *J. Phys. Chem. C* **121**, 4734 (2017).
- [18] K. E. Shulenberger, M. N. Ashner, S. K. Ha, F. Krieg, M. V. Kovalenko, W. A. Tisdale, and M. G. Bawendi, Setting an upper bound to the biexciton binding energy in CsPbBr₃ perovskite nanocrystals, *J. Phys. Chem. Lett.* **10**, 5680 (2019).
- [19] M. N. Ashner, K. E. Shulenberger, F. Krieg, E. R. Powers, M. V. Kovalenko, M. G. Bawendi, and W. A. Tisdale, Size-dependent biexciton spectrum in CsPbBr₃ perovskite nanocrystals, *ACS Energy Lett.* **4**, 2639 (2019).
- [20] I. Lindgren and J. Morrison, *Atomic Many-Body Theory*, 2nd ed. (Springer-Verlag, Berlin, 1986).
- [21] I. Shavitt and R. J. Bartlett, *Many-Body Methods in Chemistry and Physics: MBPT and Coupled-Cluster Theory* (Cambridge University Press, Cambridge, 2009).
- [22] D. M. Brink and G. R. Satchler, *Angular Momentum*, 3rd ed. (Clarendon Press, Oxford, 1994).
- [23] A. R. Edmonds, *Angular Momentum in Quantum Mechanics* (Princeton University Press, Princeton, 1960).
- [24] J. Shumway, A. Franceschetti, and A. Zunger, Correlation versus mean-field contributions to excitons, multiexcitons, and charging energies in semiconductor quantum dots, *Phys. Rev. B* **63**, 155316 (2001).
- [25] M. Kira and S. W. Koch, *Semiconductor Quantum Optics* (Cambridge University Press, New York, 2012).
- [26] R. S. Knox, *Solid State Physics*, edited by F. Seitz and D. Turnbull, Suppl. no. 5 (Academic, New York, 1963).
- [27] G. E. Pikus and G. L. Bir, Exchange interaction in excitons in semiconductors, *Zh. Eksp. Teor. Fiz.* **33**, 195 (1971).
- [28] G. B. Shaw, Degeneracy in particle-in-a-box problem, *J. Phys. A: Math. Gen.* **7**, 1537 (1974).
- [29] J. Even, L. Pedesseau, and C. Katan, Analysis of multi-valley and multibandgap absorption and enhancement of free carriers related to exciton screening in hybrid perovskites, *J. Phys. Chem. C* **118**, 11566 (2014).
- [30] M. A. Becker, R. Vaxenburg, G. Nedelcu, P. C. Serce, A. Shabaev, M. J. Mehl, J. G. Michopoulos, S. G. Lambrakos, N. Bernstein, J. L. Lyons, T. Stöferle, R. F. Mahrt, M. V. Kovalenko, D. J. Norris, G. Rainò, and A. L. Efros, Bright triplet excitons in caesium lead halide perovskites, *Nature* **553**, 189 (2018).
- [31] Z. G. Yu, Effective-mass model and magneto-optical properties in hybrid perovskites, *Sci. Rep.* **6**, 28576 (2016).
- [32] A. I. Ekimov, F. Hache, M. C. Schanneklein, D. Ricard, C. Flytzanis, I. A. Kudryavtsev, T. V. Yazeva, A. V. Rodina, and A. L. Efros, Absorption and intensity-dependent photoluminescence measurements on CdSe quantum dots—assignment of the 1st electronic-transitions, *J. Opt. Soc. Am. B* **10**, 100 (1993).
- [33] By so doing, we exclude MBPT terms involving the creation of electron-hole pairs, or *virtual excitons*, in the intermediate states. Such terms are however naturally suppressed by the small Coulomb matrix elements associated with them.
- [34] K. Chang and J. B. Xia, Spatially separated excitons in quantum-dot quantum well structures, *Phys. Rev. B* **57**, 9780 (1998).
- [35] Z. Yang, A. Surrente, K. Galkowski, A. Miyata, O. Portugall, R. J. Sutton, A. A. Haghighirad, H. J. Snaith, D. K. Maude, P. Plochocka, and R. J. Nicholas, Impact of the halide cage on the electronic properties of fully inorganic cesium lead halide perovskites, *ACS Energy Lett.* **2**, 1621 (2017).
- [36] D. N. Dirin, I. Cherniukh, S. Yakunin, Y. Shynkarenko, and M. V. Kovalenko, Solution-grown CsPbBr₃ perovskite single crystals for photon detection, *Chem. Mater.* **28**, 8470 (2016).
- [37] R. K. Singh, R. Kumar, N. Jain, S. R. Dash, J. Singh, and A. Srivastava, Investigation of optical and dielectric properties of CsPbI₃ inorganic lead iodide perovskite thin film, *J. Taiwan Inst. Chem. Eng.* **96**, 538 (2019).
- [38] P. Cottingham and R. L. Brutchey, On the crystal structure of colloiddally prepared CsPbBr₃ quantum dots, *Chem. Commun.* **52**, 5246 (2016).
- [39] C. C. Stoumpos, C. D. Malliakas, J. A. Peters, Z. Liu, M. Sebastian, J. Im, T. C. Chasapis, A. C. Wibowo, D. Y. Chung, A. J. Freeman, B. W. Wessels, and M. G. Kanatzidis, Crystal growth of the perovskite semiconductor CsPbBr₃: A new material for high-energy radiation detection, *Cryst. Growth Des.* **13**, 2722 (2013).
- [40] S. Hirotsu, J. Harada, M. Iizumi, and K. Gesi, Structural phase transitions in CsPbBr₃, *J. Phys. Soc. Jpn.* **37**, 1393 (1974).
- [41] J. Fu, Q. Xu, G. Han, B. Wu, C. H. A. Huan, M. L. Leek, and T. C. Sum, Hot carrier cooling mechanisms in halide perovskites, *Nat. Commun.* **8**, 1 (2017).
- [42] P. Umari, E. Mosconi, and F. De Angelis, Relativistic GW calculations on CH₃NH₃PbI₃ and CH₃NH₃SnI₃ perovskites for solar cell applications, *Sci. Rep.* **4**, 4467 (2014).
- [43] G. Yumoto, H. Tahara, T. Kawawaki, M. Saruyama, R. Sato, T. Teranishi, and Y. Kanemitsu, Hot biexciton effect on optical gain in CsPbI₃ perovskite nanocrystals, *J. Phys. Chem. Lett.* **9**, 2222 (2018).

- [44] Y. Dong, T. Qiao, D. Kim, D. Parobek, D. Rossi, and D. H. Son, Precise control of quantum confinement in cesium lead halide perovskite quantum dots via thermodynamic equilibrium, *Nano Lett.* **18**, 3716 (2018).
- [45] J. Pan, Y. Shang, J. Yin, M. De Bastiani, W. Peng, I. Dursun, L. Sinatra, A. M. El-Zohry, M. N. Hedhili, A.-H. Emwas, O. F. Mohammed, Z. Ning, and O. M. Bakr, Bidentate ligand-passivated CsPbI₃ perovskite nanocrystals for stable near-unity photoluminescence quantum yield and efficient red light-emitting diodes, *J. Am. Chem. Soc.* **140**, 562 (2018).
- [46] A. Dutta, S. K. Dutta, S. D. Adhikari, and N. Pradhan, *Angew. Chem. Int. Ed.* **57**, 9083 (2018).
- [47] F. Liu, Y. Zhang, C. Ding, S. Kobayashi, T. Izuishi, N. Nakazawa, T. Toyoda, T. Ohta, S. Hayase, T. Minemoto, K. Yoshino, S. Dai, and Q. Shen, Highly luminescent phase-stable CsPbI₃ perovskite quantum dots achieving near 100% absolute photoluminescence quantum yield, *ACS Nano* **11**, 10373 (2017).
- [48] C. Yin, L. Chen, N. Song, Y. Lv, F. Hu, C. Sun, W. W. Yu, C. Zhang, X. Wang, Y. Zhang, and M. Xiao, Bright-exciton fine-structure splittings in single perovskite nanocrystals, *Phys. Rev. Lett.* **119**, 026401 (2017).
- [49] D. Canneson, E. V. Shornikova, D. R. Yakovlev, T. Rogge, A. A. Mitioglu, M. V. Ballottin, P. C. M. Christianen, E. Lhuillier, M. Bayer, and L. Biadala, Negatively charged and dark excitons in CsPbBr₃ perovskite nanocrystals revealed by high magnetic fields, *Nano Lett.* **17**, 6177 (2017).
- [50] M. C. Brennan, J. E. Herr, T. S. Nguyen-Beck, J. Zinna, S. Draguta, S. Rouvimov, J. Parkhill, and M. Kuno, Origin of the size-dependent Stokes shift in CsPbBr₃ perovskite nanocrystals, *J. Am. Chem. Soc.* **139**, 12201 (2017).
- [51] This follows by putting $\gamma_e = 1$ and $\gamma_h = -1$ in A. L. Efros and M. Rosen, The electronic structure of semiconductor nanocrystals, *Annu. Rev. Mater. Sci.* **30**, 475 (2000).
- [52] The Kane parameter E_P is sometimes defined to be 1/3 of this value in the context of the $4 \times 4 \mathbf{k} \cdot \mathbf{p}$ model. See, for example, Ref. [35].
- [53] Note that in NCs of CsPbBr₃, there is a Stokes shift of the emission peak (to lower energies than the first absorption peak), which varies from a few tens of meV at the larger NC sizes $L \gtrsim 8$ nm to about 80 meV at the smaller sizes $L \approx 4$ nm; see Ref. [50]. One might also compare the theoretical single-exciton energy with the position of the first absorption peak, but the resulting change in Fig. 2 would not be very great, and it is harder to obtain experimental values for the absorption peak because few authors provide explicit peak-fits to their absorption curves.
- [54] S. Nakahara, H. Tahara, G. Yumoto, T. Kawawaki, M. Saruyama, R. Sato, T. Teranishi, and Y. Kanemitsu, Suppression of trion formation in CsPbBr₃ perovskite nanocrystals by postsynthetic surface modification, *J. Phys. Chem. C* **122**, 22188 (2018).
- [55] G. Rainò, G. Nedelcu, L. Protesescu, M. I. Bodnarchuk, M. V. Kovalenko, R. F. Mahrt, and T. Stöferle, Single cesium lead halide perovskite nanocrystals at low temperature: Fast single photon emission, reduced blinking, and exciton fine structure, *ACS Nano* **10**, 2485 (2016).
- [56] M. Fu, P. Tamarat, H. Huang, J. Even, A. L. Rogach, and B. Lounis, Neutral and charged exciton fine structure in single lead halide perovskite nanocrystals revealed by magneto-optical spectroscopy, *Nano Lett.* **17**, 2895 (2017).
- [57] R. Ben Aich, I. Saidi, S. Ben Radhia, K. Boujdaria, T. Barisien, L. Legrand, F. Bernardot, M. Chamarro, and C. Testelin, Bright-exciton splittings in inorganic cesium lead halide perovskite nanocrystals, *Phys. Rev. Appl.* **11**, 034042 (2019).
- [58] P. C. Sercel, J. L. Lyons, D. Wickramaratne, R. Vaxenburg, N. Bernstein, and A. L. Efros, Exciton fine structure in perovskite nanocrystals, *Nano Lett.* **19**, 4068 (2019).
- [59] G. D. Mahan, *Many-Particle Physics*, 3rd ed. (Kluwer Academic/Plenum Publishers, New York, 2000).
- [60] A. Karpulevich, H. Bui, Z. Wang, S. Hapke, C. P. Ramirez, H. Weller, and G. Bester, Dielectric response function for colloidal semiconductor quantum dots, *J. Chem. Phys.* **151**, 224103 (2019).
- [61] C. Katan, N. Mercier, and J. Even, Quantum and dielectric confinement effects in lower-dimensional hybrid perovskite semiconductors, *Chem. Rev.* **119**, 3140 (2019).